



# 1 Indoor Burning of Arabian Incense Generates Ultrafine-Rich 2 Particles with Strong Oxidative Potential

3

4 Liyuan Zhou<sup>1,2\*</sup>, Zhancong Liang<sup>2</sup>, Wei Xu<sup>1</sup>, Ru-Jin Huang<sup>3</sup>, Patrick K. H. Lee<sup>4</sup> and Chak K. Chan<sup>2\*</sup>

5

6 <sup>1</sup>State Key Laboratory of Advanced Environmental Technology, Institute of Urban Environment, Chinese Academy of  
7 Sciences, Xiamen 361021, China

8 <sup>2</sup>Division of Biological and Environmental Science and Engineering, King Abdullah University of Science and Technology,  
9 Thuwal, Jeddah 23955-6900, Kingdom of Saudi Arabia

10 <sup>3</sup>State Key Laboratory of Loess Science, Institute of Earth Environment, Chinese Academy of Sciences, Xi'an 710061, China

11 <sup>4</sup>School of Energy and Environment, City University of Hong Kong, Hong Kong SAR, China

12

13

14 *Correspondence to:* Liyuan Zhou (lyzhou@iue.ac.cn) and Chak K. Chan (chak.chan@kaust.edu.sa)

15

16 **Abstract.** Arabian incense (Bakhoor) burning is a widely practiced fragancing and ceremonial activity, yet how the Bakhoor  
17 composition controls particle emissions and oxidative potential remains poorly constrained, especially under repeated use in  
18 low-ventilation settings. Here we characterized emissions from Bakhoor burning in a controlled chamber using a charcoal-  
19 assisted heating configuration representative of common practice and quantified aerosol oxidative potential using  
20 complementary acellular dithiothreitol (DTT) activity and a macrophage-based intracellular oxidative-stress response, with  
21 smoldering sidestream cigarette smoke as a benchmark source. Normalized by the initial Bakhoor mass per burn, Bakhoor  
22 burning produced particle mass and number emission rates of 670-1690  $\mu\text{g min}^{-1} \text{g}^{-1}$  and  $(6-7) \times 10^{11}$  particles  $\text{min}^{-1} \text{g}^{-1}$ ,  
23 respectively. Ultrafine particles contributed 70-75% of the total particle number, and their emission rates substantially  
24 exceeded those from sidestream cigarette smoke. Across Bakhoor materials, emission magnitude followed a nonlinear power-  
25 law relationship with the loading of the hexane-soluble fraction, indicating that this fraction is an important control on particle  
26 production. In the acellular assay, the particle mass-normalized DTT consumption rate ( $\text{OP}_{\text{DTTm}}$ ) was approximately 32  $\text{pmol}$   
27  $\text{min}^{-1} \mu\text{g}^{-1}$ , modestly lower than that of cigarette smoke particles, whereas Bakhoor burning particles elicited stronger  
28 intracellular oxidative-stress responses. Ozone aging increased oxidative potential for both sources, and the acellular and  
29 cellular responses remained evident after aging equivalent to days of indoor exposure. Overall, Bakhoor burning represents a  
30 previously underrecognized source of ultrafine aerosol with substantial oxidative potential.

31

32



### 33 **1. Introduction**

34 Global exposure assessments indicate that people spend approximately 60-90% of their time indoors (Sadoun et al., 2016;  
35 Pillarisetti et al., 2022), making indoor environments an important setting for air pollutant exposure. In arid regions such as  
36 the Middle East, this percentage can approach 100% (Sadoun et al., 2016), driven by extended periods of extreme heat and  
37 limited outdoor comfort. Despite this high exposure potential, indoor air quality has historically received less scientific and  
38 regulatory attention than outdoor pollution (Cincinelli and Martellini, 2017). Indoor air is shaped by both outdoor infiltration  
39 and indoor activities, with combustion-related processes often contributing substantially to particle exposure (Gligorovski and  
40 Abbatt, 2018). While major indoor combustion sources such as tobacco smoke and household solid-fuel use have been widely  
41 studied (Wang et al., 2018a), other routine combustion-based fragancing and ceremonial practices remain comparatively  
42 under-characterized as particle sources.

43 A prominent example is the burning of Arabian incense (Bakhoor), a widely practiced fragancing and ceremonial  
44 activity in the Middle East and other regions, in which a mixture of perfumed wood chips soaked with additives is heated on  
45 charcoal. In addition to the aromatic wood chips, Bakhoor materials often contain scented oils, resins, and botanical additives  
46 such as herbs and flowers (Wahab and Mostafa, 2007), forming a chemically complex mixture that can generate condensable  
47 precursors upon thermal degradation. Because Bakhoor is typically heated on smoldering charcoal, both the Bakhoor material  
48 and the ignition source can contribute to particle formation. Bakhoor burning commonly occurs indoors, often in enclosed  
49 spaces with limited ventilation, and is embedded in daily routines as well as religious and social gatherings. In Jazan, Saudi  
50 Arabia, 98% of households report regularly burning Bakhoor indoors (Jareebi et al., 2024). Frequent incense use has also been  
51 reported in Gulf regions (Yeatts et al., 2012), while household incense burning is likewise prevalent in parts of Asia (Pan et  
52 al., 2014; Zhao et al., 2025). This widespread use indicates that combustion-based fragancing and ceremonial practices are  
53 not only regionally important, but also relevant to a broader class of indoor combustion sources. For such sources, quantitative  
54 descriptors such as source strength, particle size distribution, and particle reactivity are important for understanding emission  
55 characteristics and how they vary with source composition and burning conditions (Kuye and Kumar, 2023). Ultrafine particles  
56 are often of particular interest because of their importance to particle number emissions and their potential sensitivity to source  
57 and combustion conditions (Shen et al., 2017).

58 A limited number of studies have provided preliminary, largely qualitative evidence of potential concern related to  
59 Bakhoor burning. Elsayed et al. (2016) reported that raw, unburned Bakhoor materials contain a chemically complex mixture  
60 of organic constituents, including nitrogen-containing and other additive-related species. However, the composition of particles  
61 emitted during Bakhoor burning can differ substantially from the raw-material profile because thermochemical processing  
62 during heating and pyrolysis can transform the formulation and generate new condensable products that partition to the particle  
63 phase. Dalibalta et al. (2015) provided preliminary indications of potential concern in Bakhoor smoke by noting the presence  
64 of compounds classified as carcinogenic, toxic, and/or respiratory irritants; however, the evidence was not linked to size-  
65 resolved emissions or dose-relevant particle metrics. Alarifi et al. (2004) further reported structural changes in pneumocytes



66 following repeated animal exposure to Bakhoor smoke. Taken together, these studies suggest that Bakhoor smoke warrants  
67 further quantitative evaluation using particle-based metrics relevant to inhalation exposure.

68 Here, we characterize particle emissions and oxidative responses of Bakhoor burning in a controlled chamber, using  
69 smoldering sidestream cigarette smoke as a benchmark indoor combustion source (Chen and Zhao, 2024). Real-time particle  
70 number and mass concentrations and size distributions were measured using a scanning mobility particle sizer, and size-  
71 resolved emission factors were quantified. Particular attention was given to ultrafine particles (UFPs, <100 nm) because of  
72 their high respiratory deposition efficiency and potential relevance to systemic health effects (Oberdörster et al., 2005). Control  
73 experiments were performed to quantify the respective contributions of the Bakhoor material and the ignition charcoal to  
74 emitted particle size distributions and emission factors. Oxidative responses were evaluated using two complementary  
75 approaches commonly applied in atmospheric and exposure research (Seo et al., 2025). These included acellular oxidative  
76 potential quantified by the dithiothreitol (DTT) assay and cellular responses assessed via intracellular oxidative-stress response  
77 and cell viability in alveolar macrophages. To probe potential chemical drivers, particle extracts were analyzed offline using  
78 high-performance liquid chromatography coupled with high-resolution mass spectrometry, and compositional metrics were  
79 examined in relation to DTT activity. Changes in chemical composition and associated oxidative responses of Bakhoor burning  
80 particles were also evaluated following ozone exposure as an additional probe of post-emission processing. This work aims to  
81 better constrain the size-resolved emissions, source contributions, and oxidative responses of particles emitted from Bakhoor  
82 burning.

83

## 84 **2. Methods**

### 85 **2.1 Generation and collection of particles from Bakhoor burning and sidestream cigarette smoke**

86 All burning experiments were conducted inside a custom-built acrylic chamber (50 × 50 × 50 cm). Three commercially  
87 available Bakhoor products were purchased from local markets in Saudi Arabia, selected based on consumer popularity. For  
88 each experiment, 1 g of Bakhoor was placed onto a smoldering charcoal briquette, consistent with common household practice.  
89 The charcoal was a commercially available quick-lighting type typically used for Bakhoor burning. Charcoal-only burns were  
90 conducted under the same chamber configuration to quantify emissions attributable to the ignition source. As a benchmark,  
91 smoldering sidestream cigarette smoke was generated in the same chamber to provide a stable and continuous particle stream.  
92 Although this approach differs from puffing-based protocols, it improves reproducibility and has been used in prior emission  
93 studies (Ott et al., 2021; Wu et al., 2012). Once Bakhoor was placed on the smoldering charcoal, visible smoke generation  
94 began immediately and typically persisted for approximately 20 min. The chamber was operated under a steady-state flow-  
95 through mode with purified air supplied at 20 L min<sup>-1</sup>. Size-resolved particle number concentrations were continuously  
96 measured using a Scanning Electrical Mobility Spectrometer (SEMS; Model 2100, Brechtel Manufacturing Inc.) over a  
97 mobility diameter range of 10–500 nm. Larger particles (500–2500 nm) were quantified using an optical particle counter (OPC;  
98 Brechtel Manufacturing Inc.). Prior to each experiment, background particle concentrations in the chamber were reduced to  
99 <1 particle cm<sup>-3</sup>. Particle number size distributions from the SEMS and OPC were converted to mass concentrations assuming



100 an effective particle density of  $1 \text{ g cm}^{-3}$ . In addition to real-time measurements, aerosol samples were collected on 47 mm  
101 quartz and PTFE filters, each at approximately  $6 \text{ L min}^{-1}$  for offline chemical analysis. Quartz filters were pre-baked at  $550 \text{ }^\circ\text{C}$   
102 for 12 h to minimize background organic contamination.

### 103 **2.2 Emission rate calculations**

104 Particle mass emission rates ( $E$ ,  $\mu\text{g min}^{-1}$ ) were quantified using a size-resolved material-balance approach (Wang and Chan,  
105 2023; Jiang et al., 2021), where particle losses were treated separately for each size bin. The chamber was continuously mixed  
106 using two internal fans, and emission rates were therefore derived using a well-mixed flow-through chamber mass-balance  
107 framework. For analysis, particles were grouped into the following diameter bins: 10-100, 100-200, 200-300, 300-400, 400-  
108 500, 500-1000, 1000-1500, 1500-2000, and 2000-2500 nm.

109 For each size bin  $i$ , the time-dependent mass balance in the well-mixed chamber is

$$110 \quad V \frac{dC_i}{dt} = -F \times C_i + E_i - k_i \times V \times C_i, \quad (\text{Eq. 1})$$

111 where  $V$  is the volume of the chamber ( $\text{m}^3$ ),  $C_i$  is the mass concentration of particles in size bin  $i$  ( $\mu\text{g m}^{-3}$ ),  $F$  is the outlet airflow  
112 rate ( $\text{m}^3 \text{ min}^{-1}$ ),  $E_i$  is the particle emission rate in bin  $i$  ( $\mu\text{g min}^{-1}$ ), and  $k_i$  is the loss rate constant for particles in bin  $i$  ( $\text{min}^{-1}$ ).  
113 Particle losses were assumed to follow first-order decay, consistent with previous chamber-based emission studies (Wang and  
114 Chan, 2023). Following each Bakhoor burning event, particle concentrations exhibited near-exponential decay, which was  
115 used to estimate  $k_i$  by fitting the decay curves, following the approach described by Jiang et al. (2021). Emission rates were  
116 then integrated over the full burning period and summed across all size bins to obtain the total particulate emission rate.

### 117 **2.3 Ozone aging of particle samples**

118 To simulate oxidative aging, PM-loaded filters were placed in an in-line filter holder and exposed to a continuous flow of  
119 ozone diluted in zero air. Ozone was generated by passing zero air through a mercury lamp ozone generator (Model 610,  
120 Jelight Inc., USA), and its concentration was continuously monitored at the outlet of the filter holder using an ozone analyzer  
121 (Model 106-L, 2B Technologies Inc.). Two ozone levels were applied, approximately 200 ppb and 1500 ppb, for 30 min. These  
122 exposures correspond to approximately 20 h and 150 h of equivalent indoor ozone exposure, respectively, assuming a  
123 representative indoor ozone level of 5 ppb (Nazaroff and Weschler, 2022). This accelerated protocol was selected for  
124 practicality and reproducibility and to isolate ozone-driven processing under controlled conditions. Although filter-bound PM  
125 could, in principle, be exposed to lower ozone concentrations for longer periods, multi-day treatments increase the likelihood  
126 of uncontrolled changes that are not directly attributable to ozone, including slow volatilization of semi-volatile constituents,  
127 continued dark aging, and time-dependent particle-filter interactions. Using elevated ozone over short durations therefore  
128 enables consistent, well-defined oxidant doses while minimizing these confounding processes.

### 129 **2.4 Molecular characterization of organics in Bakhoor-burning particles**

130 To analyze the molecular composition of organic species in Bakhoor-burning particles, filter samples were extracted in  
131 acetonitrile via 30-minute sonication, followed by filtration through a  $0.22 \mu\text{m}$  PTFE syringe filter. Acetonitrile was selected  
132 over methanol to minimize solvent-induced artifacts, such as the methanolysis of conjugated carbonyl species (Chen et al.,



133 2022). The extracts were analyzed using ultra-high-performance liquid chromatography coupled with high-resolution Orbitrap  
134 mass spectrometry (UHPLC-HRMS; Orbitrap ID-X, Thermo Fisher Scientific Inc.), equipped with an electrospray ionization  
135 (ESI) source operated in positive ion mode. Chromatographic separation was performed on an Acquity HSS T3 column (1.8  
136  $\mu\text{m}$ , 2.1 mm  $\times$  100 mm; Waters Corp.) under conditions optimized for semi-polar organic compounds (Wang et al., 2021; Go  
137 et al., 2022). The liquid chromatography gradient and flow parameters were configured to improve separation efficiency and  
138 minimize matrix effects, following established protocols for analyzing dissolved organic matter and aerosol extracts (Go et al.,  
139 2022; Liang et al., 2024; Patriarca et al., 2018). Data acquisition and molecular formula assignment were conducted using  
140 Compound Discoverer software (Thermo Fisher Scientific Inc.), with elemental compositions determined from exact  $m/z$   
141 values and isotopic patterns. This analytical workflow enabled untargeted molecular profiling of the complex organic mixtures  
142 emitted from Bakhoor burning.

### 143 **2.5 Acellular dithiothreitol (DTT) assay**

144 The oxidative potential of particulate matter is a key indicator of its capacity to generate reactive oxygen species (ROS) and  
145 induce oxidative stress (Jiang et al., 2019). Among acellular assays, the DTT assay is widely used as a proxy for particle redox  
146 activity and quantification of the rate of DTT consumption by redox-active species that catalyze electron-transfer reactions  
147 (Cho et al., 2005). The experimental protocol followed established methods reported previously (Gao et al., 2017; Fang et al.,  
148 2017; Lyu et al., 2018; Cho et al., 2005). Briefly, filter samples were extracted in deionized water by 30 minutes of sonication.  
149 Given the potential for radical formation during sonication, a comparison between sonication and vortex shaking was  
150 conducted. The results showed no significant difference in DTT consumption, indicating that sonication did not introduce  
151 measurable artifacts. For the measurement of water-soluble oxidative potential ( $\text{OP}^{\text{WS-DTT}}$ ), the extract was filtered and 0.7 mL  
152 of the filtrate was mixed with 0.1 mL of 1 mM DTT solution and 0.2 mL of potassium phosphate buffer (0.5 M, pH 7.4). The  
153 mixture was incubated at 37 °C in a thermostatic shaker with continuous agitation. At designated time points (0, 5, 10, 15, 25,  
154 and 35 minutes), 0.1 mL aliquots were withdrawn and quenched by adding trichloroacetic acid (TCA). The residual DTT in  
155 each aliquot was then reacted with Tris buffer (0.4 M containing 20 mM EDTA) and 5,5'-dithiobis-(2-nitrobenzoic acid)  
156 (DTNB). The reaction yields a yellow chromophore that absorbs at 412 nm, which was quantified using a microplate reader.  
157 To determine the total oxidative potential ( $\text{OP}^{\text{Total-DTT}}$ ), the same procedure was used, except the extract was not filtered, and  
158 the filter itself remained in the reaction mixture. This ensured that DTT-active species associated with insoluble particles  
159 suspended in the extract or still attached to the filter surface were also included in the measurement (Fang et al., 2017; Gao et  
160 al., 2017). To minimize photo-degradation of DTT and DTNB, all procedures were performed under low-light conditions by  
161 minimizing workspace lighting and covering vials with aluminum foil when not in use.

### 162 **2.6 Cellular macrophage assays**

163 Alveolar macrophages represent the first line of defense in the respiratory system and are widely used to assess oxidative and  
164 toxicological responses to PM exposure, particularly through intracellular ROS generation (Liu et al., 2023; Liu et al., 2020b;  
165 Liu et al., 2020a; Tuet et al., 2019). In this study, murine alveolar macrophages (MH-S, ATCC CRL-2019) were cultured in  
166 RPMI-1640 medium (ATCC) supplemented with 10% fetal bovine serum (FBS; VWR), 1% penicillin–streptomycin (Pen-



167 Strep; VWR), and 50  $\mu\text{M}$   $\beta$ -mercaptoethanol (BME; Sigma-Aldrich). Cells were maintained at 37 °C in a humidified 5% CO<sub>2</sub>  
168 incubator. Prior to ROS measurements, 96-well plates were pre-coated with 10% FBS in phosphate-buffered saline (PBS) to  
169 promote cell adherence. MH-S cells were seeded at a density of  $2 \times 10^4$  cells per well and incubated with the ROS-sensitive  
170 fluorescent probe carboxy-H<sub>2</sub>DCFDA (Molecular Probes, C-400). To introduce particulate exposure, PTFE filters loaded with  
171 either fresh or ozone-aged Bakhoor burning particles were directly immersed in the culture medium. A 3-minute vortex mixing  
172 step was applied to enhance dispersion of PM into the media. Cells were exposed for 24 hours, after which the filters were  
173 removed and intracellular oxidative-stress responses were measured using a microplate reader (excitation/emission: 485/525  
174 nm). All treatments were conducted in triplicate using independent filter samples. Blank controls (media only, no PM) were  
175 used to normalize fluorescence values.

176 A mitochondrial dehydrogenase (MTT) assay was conducted to evaluate cell viability following 24-hour exposure to  
177 PM. After exposure, the culture medium in each well was replaced with 100  $\mu\text{L}$  of fresh medium, and 10  $\mu\text{L}$  of MTT solution  
178 ( $5 \text{ mg mL}^{-1}$ ) was added. Cells were incubated for an additional 4 hours at 37 °C to facilitate the formation of purple formazan  
179 crystals. Following this, 100  $\mu\text{L}$  of a solubilization solution consisting of 10% SDS in 0.01 M HCl was added to each well,  
180 and incubation was continued for a further 15–18 hours under the same conditions. The absorbance at 570 nm was then  
181 measured using a microplate reader to quantify formazan formation, which serves as an indicator of mitochondrial enzymatic  
182 activity and, consequently, cell viability. A viability calibration curve was established by preparing mixtures of live and heat-  
183 inactivated (autoclaved) cells at defined ratios, treating them with the same MTT procedure, and recording their absorbance at  
184 570 nm to relate optical density to cell survival.

185

### 186 3. Results and discussion

#### 187 3.1 Emission characteristics of Bakhoor burning particles

188 Figure 1A-B show the size distributions of particle number and mass for emissions from Bakhoor burning, with smoldering  
189 sidestream cigarette smoke included as a comparative benchmark. Because Bakhoor was heated on a smoldering charcoal  
190 briquette, the measured distributions reflect combined contributions from the Bakhoor material and the ignition source. A  
191 charcoal-only control is therefore included to isolate charcoal-derived emissions. In the number distribution (Figure 1A),  
192 charcoal-only burning produced a weak nucleation-mode signal largely confined to the ultrafine range, whereas Bakhoor  
193 burned on charcoal yielded substantially higher concentrations and a bimodal profile, with a dominant ultrafine mode near 30  
194 nm and a secondary mode around 160 nm. The ultrafine-mode peak was approximately 1.4 times the secondary peak, indicating  
195 strong enrichment of ultrafine particles (UFPs, <100 nm) by number. Sidestream cigarette smoke, by comparison, exhibited a  
196 unimodal number distribution centered at approximately 110 nm under the protocol used here, with a substantially lower UFP  
197 contribution. In the mass distribution (Figure 1B), Bakhoor burning produced a unimodal profile centered at approximately  
198 350 nm, indicating that emitted mass was dominated by accumulation-mode particles. Time-resolved measurements further  
199 show that particle concentrations rose within seconds after ignition, peaked at approximately 5 min, and then decayed (Figure  
200 1C).



201 Figure 1D summarizes emission rates normalized to the initial Bakhoor mass per burn and to the mass of cigarette  
202 tobacco filler consumed in the sidestream benchmark. On this basis, Bakhoor burning produced particle mass emission rates  
203 of 670-1690  $\mu\text{g min}^{-1} \text{g}^{-1}$ , substantially higher than the sidestream cigarette benchmark ( $\sim 250 \mu\text{g min}^{-1} \text{g}^{-1}$ ). Because the  
204 cigarette benchmark was generated without active puffing, the resulting emission factors provide a conservative reference  
205 relative to active smoking conditions reported in the literature (Hu et al., 2023). In the context of typical indoor sources, these  
206 mass emission rates place Bakhoor burning toward the upper end of reported emission rates for activities including tobacco  
207 and incense burning, moxa, candles, and non-combustion sources such as cooking and e-cigarettes ( $117\text{--}3367 \mu\text{g min}^{-1}$ ), while  
208 recognizing that reported rates can vary with experimental configuration and normalization (Hu et al., 2023; Chuang et al.,  
209 2013; Jetter et al., 2002; Tian et al., 2021). Unlike conventional incense burning, however, Bakhoor combines a charcoal  
210 ignition source with a chemically complex mixture of perfumed wood and additives. Number-based emission rates for Bakhoor  
211 reached  $(6\text{--}7)\times 10^{11}$  particles  $\text{min}^{-1} \text{g}^{-1}$ , with UFPs accounting for 70–75% of total number, compared with  $\sim 47\%$  for the  
212 cigarette benchmark. Taken together, these results identify Bakhoor burning as a high-intensity indoor particle source that is  
213 strongly enriched in UFPs by number while also producing substantial fine-particle mass emissions.

### 214 **3.2 The potential drivers of particle formation during Bakhoor burning**

215 Figure 2A shows that charcoal-only burning produces a short-lived nucleation-mode signal immediately after ignition that  
216 decays rapidly, whereas Bakhoor burning sustains elevated particle concentrations and extends to larger particle diameters.  
217 This contrast indicates that particle formation is not controlled by the ignition source alone, but depends strongly on the  
218 Bakhoor material itself. To identify the Bakhoor components responsible for this behavior, Bakhoor materials were  
219 operationally separated into the hexane-soluble fraction (HSF) and the wood residue. The HSF is a solvent-defined operational  
220 fraction containing hexane-soluble organic material, which may include fragrance oils, resins, and related additives. The  
221 residue represents the nonextractable wood matrix. Burning the corresponding wood residues yielded nearly identical particle  
222 mass emission rates across the three Bakhoor types, whereas the original Bakhoor materials varied by approximately 2.5-fold  
223 in mass emission rates (Figure 2B). This contrast indicates that the observed differences among commercial products are  
224 primarily driven by the HSF rather than by the base wood substrate under the conditions used here. To verify that solvent  
225 extraction did not alter the wood matrix and independently affect emissions, we conducted a reconstitution experiment in  
226 which the HSF was recombined with the wood residue at the appropriate mass fractions. The reconstituted material reproduced  
227 particle mass emission rates similar to those of the original samples (Figure S3), further indicating that the observed differences  
228 are driven primarily by the presence or absence of the HSF rather than by extraction-induced changes to the wood substrate.

229 Across the original Bakhoor samples, the HSF loading (9-22% by mass) was strongly associated with particle mass  
230 emissions (Figure 2B), with Type 2 exhibiting both the highest HSF loading and the highest mass emission rate. Perturbation  
231 experiments that partially reduced the HSF (tissue wiping) and increased it by recombining the HSF with the wood residue  
232 collapsed onto a common relationship between emission rate and HSF loading across all Bakhoor types. This relationship  
233 supports HSF loading as the primary control on emission magnitude, even though the composition of the HSF varied slightly  
234 among samples (Figure S4). This dependence was well described by a power-law relationship ( $\beta \approx 2.1$ ; Figure 2B),



235 demonstrating a nonlinear response in which emissions increase more steeply as the HSF increases. Adding HSF to reach  
236 approximately 10 wt % of the reconstructed material increased mass emission rates by  $\sim 1.7$ -fold, whereas increasing the HSF  
237 content to approximately 20 wt % increased emissions by  $\sim 4.3$ -fold. This pattern suggests a threshold-like increase in effective  
238 particle formation efficiency, where incremental increases in available precursors result in disproportionate increases in  
239 particle production (Zhang et al., 2010).

240 Thermogravimetric analysis (TGA) was used to assess whether the observed HSF dependence could be primarily  
241 explained by simple evaporation of intact additives. Across the three Bakhoor types, thermograms were similar and showed  
242 only minor mass loss (approximately 5%) below 100-120 °C (Figure S5), whereas most mass loss occurred between  
243 approximately 150 and 350 °C. Thermocouple measurements showed that the charcoal temperature reached approximately  
244 300 °C within 15 s of sustained ignition in our setup (Figure S6), suggesting that Bakhoor materials are quickly driven into a  
245 higher-temperature regime rather than remaining in a low-temperature evaporation window. The reported onset of wood  
246 pyrolysis (approximately 180 °C) refers primarily to the lignocellulosic wood substrate (Escalante et al., 2022). In contrast,  
247 the HSF consists of nonstructural, solvent-extractable organics introduced during product formulation, which may volatilize  
248 and thermally transform over overlapping temperature windows during heating on charcoal. Taken together, these results  
249 suggest that HSF-linked particle formation is not solely explained by low-temperature evaporation and likely involves  
250 thermochemical processing during heating that generates condensable products, as illustrated in Figure 2C. Because TGA does  
251 not provide a mass balance for emitted particles, it is used here to bracket plausible precursor-generation regimes rather than  
252 to quantify particle yields.

### 253 **3.3 Oxidative potential of particles from Bakhoor burning**

254 To evaluate the oxidative potential of particles emitted from Bakhoor burning, we applied the dithiothreitol (DTT) assay. We  
255 report the particle mass-normalized DTT consumption rate ( $OP_{DTTm}$ ,  $\text{pmol min}^{-1} \mu\text{g}^{-1}$ ) for both filtered aqueous extracts and  
256 total (unfiltered) aqueous suspensions to gauge the relative contributions of water-soluble versus suspension-associated  
257 components. Fresh Bakhoor extracts exhibited an average  $OP_{DTTm}$  of approximately  $32 \text{ pmol min}^{-1} \mu\text{g}^{-1}$  (Figure 3A). This  
258 magnitude lies within reported ranges for laboratory-generated particles from indoor combustion sources ( $8\text{-}95 \text{ pmol min}^{-1} \mu\text{g}^{-1}$ ;  
259 Hu et al., 2023; Zhang et al., 2024) and for raw wood/biomass materials such as pine ( $35\text{-}117 \text{ pmol min}^{-1} \mu\text{g}^{-1}$ ; Zhang et al.,  
260 2024), and is comparable to values reported for ambient PM and biomass-burning organic aerosol fractions. Notably, the  
261  $OP_{DTTm}$  of Bakhoor burning particles exceeds the typical range for wildfire-influenced PM ( $2\text{-}16 \text{ pmol min}^{-1} \mu\text{g}^{-1}$ ; Fang et al.,  
262 2023), reaching values near the upper end of the wildfire range (around  $32 \text{ pmol min}^{-1} \mu\text{g}^{-1}$ ; Isenor et al., 2025). Under the  
263 same assay conditions, cigarette smoke particles showed a higher  $OP_{DTTm}$  of approximately  $50 \text{ pmol min}^{-1} \mu\text{g}^{-1}$ , about 40%  
264 higher than Bakhoor burning particles. To assess the contribution of insoluble components,  $OP_{DTTm}$  was also measured for  
265 total particle suspensions (Fang et al., 2023; Charrier and Anastasio, 2012; Brehmer et al., 2019). Only a modest enhancement  
266 (approximately 10%) was observed relative to filtered extracts (Figure 3A), suggesting that DTT-reactive species are captured  
267 predominantly in the aqueous phase under the extraction conditions used here.



268 Oxidative aging can further shape exposure-relevant redox properties because indoor oxidants can transform particle  
269 composition and, in turn, DTT consumption (Wong et al., 2019; Wang et al., 2023). Given the limited penetration of shortwave  
270 UV radiation indoors, we focus here on ozone-driven aging (Wang et al., 2018a; Yuan et al., 2025). Residential air exchange  
271 rates typically range from 0.05 to 1 h<sup>-1</sup> (Zhao and Liu, 2020; Salthammer, 2011), corresponding to ventilation-based particle  
272 residence times of approximately 1-20 h. Moreover, the high indoor surface-to-volume ratio promotes rapid particle deposition  
273 to surfaces (Abbatt and Wang, 2020), creating reservoirs that are not removed by ventilation and can persist for days; these  
274 deposits can continue to undergo chemical processing and may contribute to exposure through subsequent resuspension or  
275 disturbance of indoor surfaces. After an ozone dose equivalent to approximately 150 h at an indoor ozone level of 5 ppb (Figure  
276 3B), OP<sub>DTTm</sub> for water extracts increased by approximately 15% for both Bakhoor and cigarette smoke particles. This increase  
277 suggests the net formation of more DTT-active oxygenated products during ozonolysis, consistent with a rise in the carbon  
278 oxidation state (OSc) derived from mass spectrometric analysis (Figures S7 and S8). Across fresh and O<sub>3</sub>-aged samples, the  
279 median OP<sub>DTTm</sub> of Bakhoor water extracts fell within the broad range reported for laboratory combustion-derived PM and  
280 overlapped values reported for field PM, although many field studies report total OP<sub>DTTm</sub>, which is typically higher than the  
281 water-soluble fraction. Prior work by Wong et al. (2019) reported an initial increase in OP<sub>DTTm</sub> (~20%) during the early stages  
282 of ozonolysis of biomass-burning particles, followed by a decrease toward baseline after extended aging (up to 70 h),  
283 suggesting that some DTT-active products can be transient. Quinone-like redox-cycling species, which catalyze ROS  
284 formation, have been proposed as plausible contributors to the observed changes in oxidative potential (Xiong et al., 2017).  
285 These observations motivate identifying the chemical drivers that govern DTT consumption in Bakhoor smoke.

### 286 3.4 Potential chemical contributors to DTT activity

287 To examine which particle-phase constituents may underlie the observed DTT response, we analyzed extracts of Bakhoor  
288 burning and cigarette smoke particles using UHPLC-HRMS. Both sources showed broad distributions of detected features  
289 spanning  $m/z \approx 100-400$  (Figure S9), consistent with LC/ESI-MS characterizations of biomass-burning organic aerosol and  
290 combustion-derived organic aerosol (Smith et al., 2009). Despite comparable  $m/z$  envelopes, the assigned elemental-  
291 composition classes differed markedly between the two sources. Bakhoor burning particles were dominated by CHO formulas  
292 (~65% of assigned species), whereas cigarette smoke particles were relatively less oxygenated and strongly enriched in  
293 nitrogen-containing formulas (CHN+CHON≈84%) (Figure S9). Since elemental class alone provides limited insight into  
294 structural motifs relevant to redox cycling, we also computed the modified aromaticity index (AI<sub>mod</sub>, see Text S1 for details)  
295 as a proxy for unsaturation and aromatic character and classified formulas as aromatic (AI<sub>mod</sub> ≥ 0.5), olefinic (0 < AI<sub>mod</sub> < 0.5),  
296 or aliphatic (AI<sub>mod</sub> = 0) (Koch and Dittmar, 2006; Song et al., 2021; Song et al., 2019).

297 We then related OP<sub>DTTm</sub> to molecular-formula-derived metrics (AI<sub>mod</sub>, O:C, N:C) across fresh and ozone-aged samples  
298 from both sources (Figure 4). Across the full dataset, aromatic-like formulas (AI<sub>mod</sub> ≥ 0.5) exhibited the strongest positive  
299 association with OP<sub>DTTm</sub> (R<sup>2</sup> > 0.5). The strongest correlations were observed for moderately oxygenated formulas (O:C ≈ 0.05-  
300 0.15), indicating that the DTT response likely tracks most closely with unsaturated/aromatic-like formulas and is consistent  
301 with the O:C range often associated with redox-active aromatic products, including quinone-like structures (Charrier and



302 Anastasio, 2012). In contrast, highly oxidized formulas (e.g., acid-rich CHO species at higher O:C) and aliphatic-like formulas  
303 ( $AI_{\text{mod}} = 0$ ) showed weaker associations with  $OP_{\text{DTTm}}$  (Shultz et al., 2011; Park et al., 2006). These interpretations are based on  
304 molecular formulas and bulk metrics. Definitive assignment to specific compound classes (e.g., individual quinones) requires  
305 targeted identification and standards.

306 Nitrogen-containing aromatic-like formulas also exhibited positive associations with  $OP_{\text{DTTm}}$ , with the strongest  
307 relationships observed at  $N:C \approx 0.10-0.25$ . Because the strongest correlations overall occurred for aromatic-like formulas with  
308 high  $AI_{\text{mod}}$ , this pattern suggests that nitrogen substitution within unsaturated/aromatic-like structures may mark an additional  
309 set of formulas associated with DTT activity at the molecular-formula level. The intrinsic DTT reactivity of individual  
310 nitrogen-containing organics remains less well constrained than that of quinone-type species, but prior work has linked  
311 nitroaromatics and N-heterocycles to enhanced DTT responses in complex mixtures (Lai et al., 2025). Nitrogen functionalities  
312 may also influence redox cycling indirectly, for example by modulating electron density or stabilizing redox intermediates in  
313 mixed organic matrices (Dou et al., 2015). Consistent with these associations, Bakhoor-burning particles were dominated by  
314 CHO formulas and only a minority met the aromatic-like criterion ( $AI_{\text{mod}} \geq 0.5$ ; Figure S11), whereas a substantially larger  
315 fraction of cigarette-derived CHN/CHON formulas were aromatic-like (Figure S11), corresponding to the higher  $OP_{\text{DTTm}}$   
316 observed for cigarette smoke particles.

317 Finally, since dissolved transition metals can contribute to DTT activity directly and/or via interactions with organics  
318 (Jiang et al., 2019; Wang et al., 2018b), we conducted metal-chelation tests using Chelex resin.  $OP_{\text{DTTm}}$  changed negligibly  
319 after chelation (Figure S12), indicating a minimal contribution from dissolved metals and suggesting that  $OP_{\text{DTTm}}$  in both  
320 sources is dominated by organic species.

### 321 3.5 Cellular oxidative-stress responses induced by Bakhoor burning particles

322 To further assess cellular oxidative-stress responses to Bakhoor burning particles, we quantified intracellular fluorescence  
323 signals in alveolar macrophages using a DCFH-based assay and reported responses as fold changes relative to untreated  
324 controls. This cellular endpoint complements the acellular DTT assay by capturing integrated intracellular oxidant signaling  
325 under particle exposure. As described in the Methods, five particle dose levels were tested for each sample, dose-response  
326 relationships were fitted using the Hill equation, and the area under the fitted dose-response curve (AUC) was used as an  
327 integrative metric to quantify the overall oxidative response (Figure 5A) (Tuet et al., 2016).

328 Bakhoor burning particles elicited stronger DCFH fluorescence responses than sidestream cigarette smoke particles  
329 across the tested dose range (Figure 5B). The AUC metric ranged from 0.51 to 0.62 for Bakhoor samples, higher than 0.41 for  
330 cigarette smoke. The magnitude of the response induced by Bakhoor burning particles was comparable to that reported for  
331 naphthalene-derived secondary organic aerosol, a well-established oxidative-stress inducer in cellular assays (Tuet et al.,  
332 2017). At higher particle doses, the fluorescence response approached a plateau (Figure 5A), consistent with saturation of the  
333 assay response and/or the onset of cytotoxicity, as supported by the accompanying MTT viability results (Figure S13).

334 Notably, these cellular oxidative-stress responses differed from the acellular DTT results, for which cigarette smoke  
335 particles exhibited 47-100% higher  $OP_{\text{DTTm}}$  than Bakhoor burning particles. Such divergence is expected because DTT and



336 DCFH-based cellular readouts probe different chemical and biological processes and can be weakly correlated for complex  
337 mixtures (Kim et al., 2014; Tuet et al., 2016; Seo et al., 2025). Similar assay-dependent discrepancies have been reported  
338 previously; for example, Tuet et al. (2016) observed weak or absent correlations between DTT activity and DCFH-based  
339 cellular oxidative-stress responses for some wintertime ambient PM samples. Mechanistically, DTT primarily reflects the  
340 electron-transfer capacity of extractable species in a simplified buffer system, whereas the cellular assay integrates particle  
341 delivery and uptake, intracellular bioactivation, depletion of redox buffers, and activation of oxidant-generating pathways  
342 (Kim et al., 2014). Collectively, these results underscore that DTT alone may not capture the full spectrum of oxidative-stress  
343 potential for indoor combustion aerosols.

344 Although mechanistic attribution of cellular signaling to specific molecules is inherently challenging, the  
345 compositional information provides plausible hypotheses for why Bakhoor burning particles produced stronger cellular  
346 oxidative-stress responses. Bakhoor extracts were enriched in oxygenated CHO formulas (Figures S9 and S10), consistent  
347 with a larger contribution from oxygenated organics, some of which may contain electrophilic carbonyl functionality.  
348 Electrophilic aldehydes and related carbonyls are well known to form covalent adducts with cellular nucleophiles, particularly  
349 cysteine thiols in glutathione and proteins, thereby depleting intracellular thiol buffering capacity and perturbing redox  
350 homeostasis in ways that can amplify downstream oxidant signaling (Fritz and Petersen, 2013; Lopachin and Gavin, 2014).  
351  $AI_{mod}$  classification further places a substantial fraction of Bakhoor CHO formulas in the olefinic and non-aromatic unsaturated  
352 regimes (Figure S11). These less-condensed CHO structures may be more conformationally flexible than condensed aromatic  
353 frameworks and may interact differently with lipid phases, potentially affecting cellular delivery and subsequent bioactivation  
354 (Liu et al., 2011). By contrast, cigarette smoke particles were enriched in nitrogen-containing formulas (CHN/CHON, Figure  
355 S11) yet produced a lower net DCFH response under the exposure conditions used here, suggesting that the dominant chemical  
356 drivers of  $OP_{DTTm}$  and cellular oxidative-stress responses differ across sources.

357

#### 358 **4. Conclusions and atmospheric implications**

359 This study demonstrates that Bakhoor burning is a potent indoor source of fine particles, particularly with a substantial ultrafine  
360 fraction. Across the three products tested here, Bakhoor burning produced particle mass and number emission rates of 670-  
361  $1690 \mu\text{g min}^{-1} \text{g}^{-1}$  and  $(6-7) \times 10^{11} \text{ particles min}^{-1} \text{g}^{-1}$ , respectively, with ultrafine particles accounting for 70-75 % of total  
362 particle number. On a mass-normalized basis, these emission rates were approximately 4.3-fold higher than those of the  
363 sidestream cigarette benchmark. Together with the observed size distributions, these results indicate that routine Bakhoor use  
364 can generate exposure-relevant particle burdens comparable to, and in some use scenarios exceeding, those from more widely  
365 recognized indoor combustion sources. Because respiratory deposition varies strongly with particle diameter and differs  
366 between the tracheobronchial (Tb) and alveolar (Al) regions (Figures 6A and 6B), lung-deposited surface area (LDSA; see  
367 Text S2) was estimated as an inhalation-relevant dose metric that has been shown to track inflammatory and cytotoxic  
368 responses across particle types more consistently than particle mass alone (Hofmann, 2011; Oh et al., 2023). Using the mean  
369 emission factors measured here together with size-resolved regional deposition fractions from Hofmann (2011), the Bakhoor-



370 to-cigarette LDSA ratio exhibits strong size dependence and reaches its highest values in the ultrafine range (Figure 6B).  
371 Because particles at intermediate diameters dominate the emitted size distribution and the integrated surface-area dose (Figure  
372 S14), the LDSA ratio integrated over the measured size range is approximately 4 for both the Tb and Al regions (Figure 6C).  
373 For a reported Bakhhor use rate of 0.4-2.9 g d<sup>-1</sup> (Bu-Olayan and Thomas, 2021), this scaling suggests that the daily inhalation-  
374 relevant dose from Bakhhor burning may be comparable to that from multiple cigarettes of smoldering sidestream smoke under  
375 the benchmark conditions used here, although the real-world equivalence will vary with room volume, ventilation, and burning  
376 practice.

377         Across the samples tested here, the combination of acellular OP<sub>DTM</sub> and macrophage DCFH responses shows that  
378 Bakhhor burning particles exhibit substantial oxidative potential and cellular oxidative-stress responses. Relative to sidestream  
379 cigarette smoke particles, these responses differ between assays on a per-mass basis and persist after ozone aging over multi-  
380 day equivalent exposures. Fresh Bakhhor extracts showed an average OP<sub>DTM</sub> of approximately 32 pmol min<sup>-1</sup> µg<sup>-1</sup>, ozone  
381 aging increased OP<sub>DTM</sub> by about 15 % under the conditions used here, and the DCFH-based AUC values for Bakhhor samples  
382 ranged from 0.51 to 0.62, compared with 0.41 for the cigarette benchmark. These results suggest that the oxidative properties  
383 of Bakhhor-burning particles can remain relevant after post-emission aging, rather than being limited to freshly emitted  
384 particles alone. This may be particularly important in indoor environments with limited ventilation and repeated daily use,  
385 where particle accumulation and continued chemical processing by indoor oxidants and surface interactions may extend the  
386 relevance of these responses beyond the point of emission. Such conditions are especially relevant in hot-arid regions such as  
387 the Middle East, where indoor spaces are frequently cooled using air-conditioning systems and windows may remain closed;  
388 in many settings with limited outdoor-air supply, air-exchange rates can be low (for example, <0.5 h<sup>-1</sup>) (Indraganti et al., 2016;  
389 Diapouli et al., 2013). The accompanying reduction in cell viability further suggests that these oxidative responses may be  
390 associated with measurable biological effects under the in vitro exposure conditions tested here. Relating these in vitro  
391 exposure conditions to human lung dose, however, will require dedicated dosimetry and exposure modeling and should be  
392 addressed in future work.

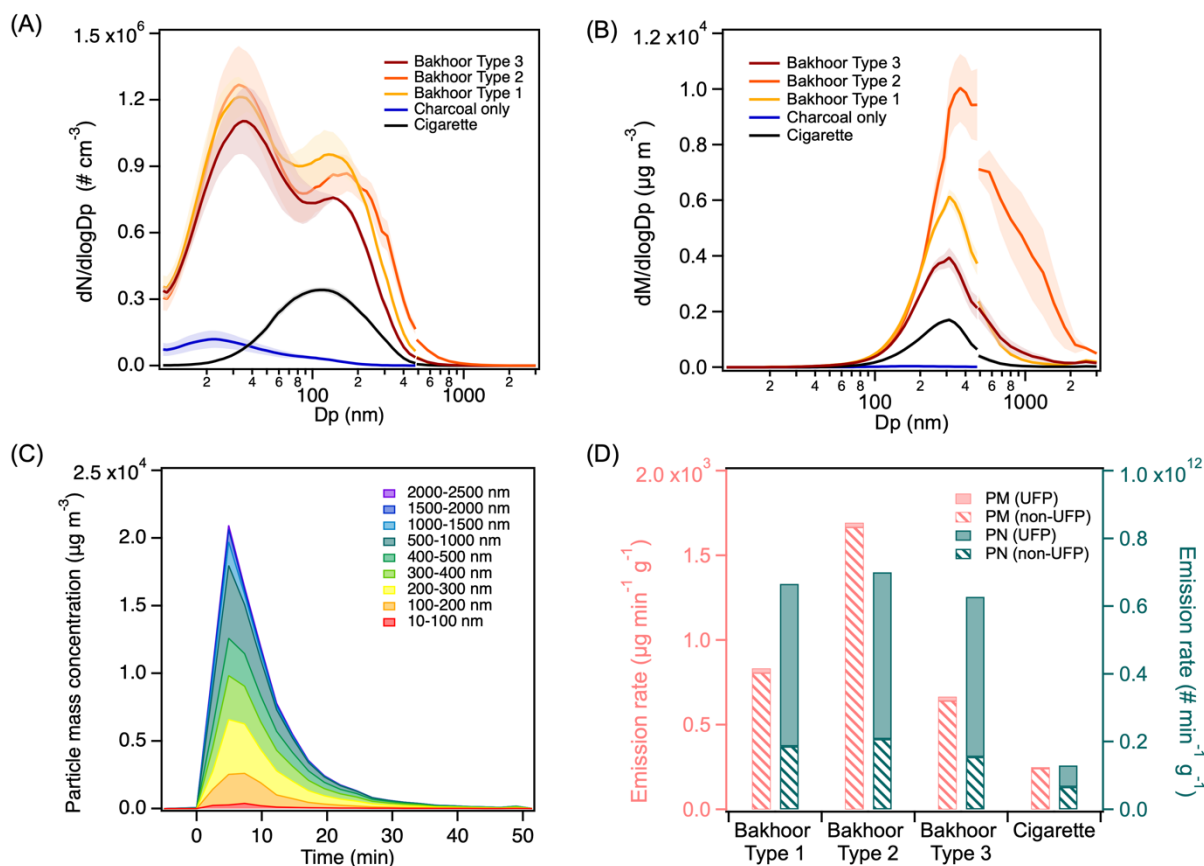
393         The control and perturbation experiments further identify the hexane-soluble fraction (HSF) as an important leverage  
394 point for particle formation during Bakhhor burning. Operational treatments that reduced the HSF, including solvent extraction  
395 to generate wood residue and a simple tissue-wiping step to partially remove surface-associated HSF, lowered particle mass  
396 emissions. However, these perturbations yielded slightly higher particle mass-normalized OP<sub>DTM</sub> relative to untreated material  
397 (Figure S15), indicating that emission reductions do not necessarily lead to a reduction in oxidative potential on a mass basis.  
398 Nevertheless, when OP<sub>DTM</sub> is combined with the corresponding emission factors to estimate emission-weighted total DTT  
399 consumption, the net oxidative burden decreases for the HSF-reduced treatments (Figure S15). These results indicate that the  
400 HSF strongly influences both emission magnitude and oxidative properties. Because HSF loading varies across products,  
401 lowering HSF loading may provide a practical pathway to reduce emitted particle mass and, consequently, exposure, although  
402 hazard-relevant endpoints should be evaluated in parallel rather than inferred from emissions alone. At the user level, wiping  
403 Bakhhor pieces prior to burning may partially remove surface-associated HSF and reduce emissions, although the effectiveness



404 of this measure will likely vary across products and user practice and should be quantified under realistic operating conditions.  
405 Electric Bakhoo burners may also represent a useful alternative by eliminating charcoal-assisted combustion and potentially  
406 reducing combustion-related particle formation, but their net effects on emissions and toxicity require evaluation under realistic  
407 use conditions before broad recommendations can be made. More broadly, these results identify source composition and  
408 burning configuration as important controls on particle emissions from Bakhoo burning, while highlighting the additional role  
409 of ventilation in shaping real-use exposure.  
410



411



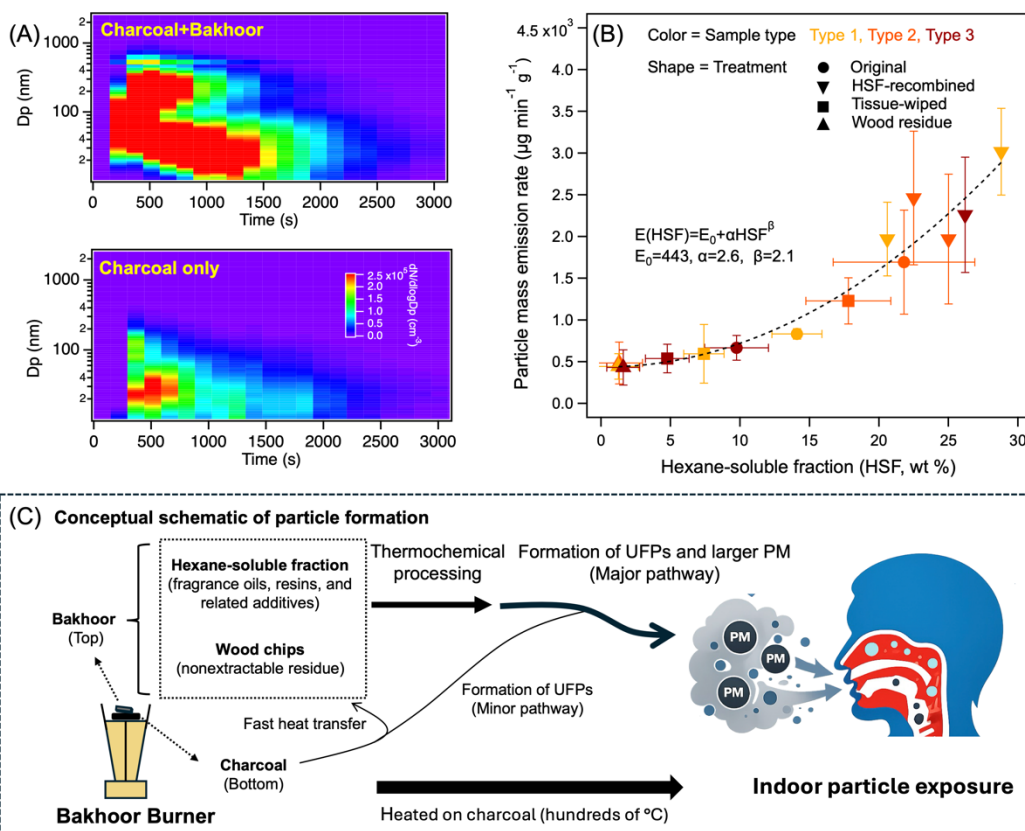
412 **Figure 1.** (A) Number and (B) mass size distributions measured in the chamber during Bakhoor burning on charcoal (three  
 413 products) and smoldering sidestream cigarette smoke, with a charcoal-only control; distributions are shown without size-  
 414 dependent loss correction. (C) Average particle mass concentration as a function of time following Bakhoor burning, resolved  
 415 by particle size ranges and shown without loss correction. (D) Particle emission rates, with mass (left axis) and number (right  
 416 axis) normalized to the initial Bakhoor mass per burn and to the mass of cigarette tobacco filler, respectively, reported  
 417 separately for ultrafine and non-ultrafine size fractions and corrected for size-dependent losses. The apparent discontinuity  
 418 near 500 nm in panels A and B reflects the use of two instruments: particles below 500 nm were measured by the SEMS,  
 419 whereas particles above 500 nm were measured by the OPC.

420

421

422

423

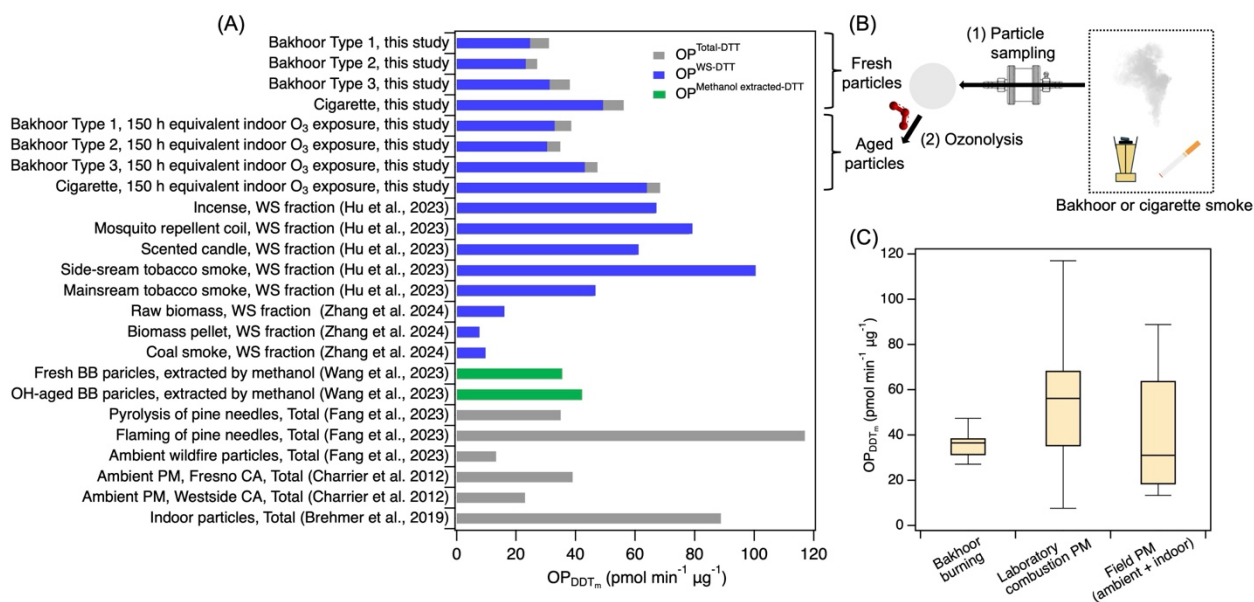


424

425 **Figure 2.** (A) Time-resolved particle number size distributions (dN/dlogD<sub>p</sub>) measured during Bakhoor burning (with charcoal  
 426 used for ignition) and during a charcoal-only control, shown as contour maps of mobility diameter (D<sub>p</sub>) versus time. (B) Particle  
 427 mass emission rate as a function of the loading of the hexane-soluble fraction (HSF, wt %) in Bakhoor materials. Colors denote  
 428 Bakhoor type, and symbols denote treatment (original, HSF-recombined, tissue-wiped, and wood residue). The dashed curve  
 429 shows an empirical fit,  $E(\text{HSF}) = E_0 + \alpha \text{HSF}^\beta$  (parameters shown). (C) Conceptual schematic linking Bakhoor composition  
 430 and heating on charcoal to fine particle formation and indoor particle exposure.



431



432 **Figure 3.** (A) The mass-normalized DTT consumption rate ( $OP_{DDT_m}$ ) for Bakhoor burning and sidestream cigarette smoke

433 particles in this study (fresh and ozone-aged), shown alongside literature values for other laboratory combustion aerosols and

434 field PM. (B) Schematic of particle collection on filters and subsequent ozonolysis of PM-loaded filters prior to DTT analysis.

435 (C) Box plot summarizing  $OP_{DDT_m}$  grouped as Bakhoor burning, other laboratory combustion PM and field PM.

436

437

438

439

440

441

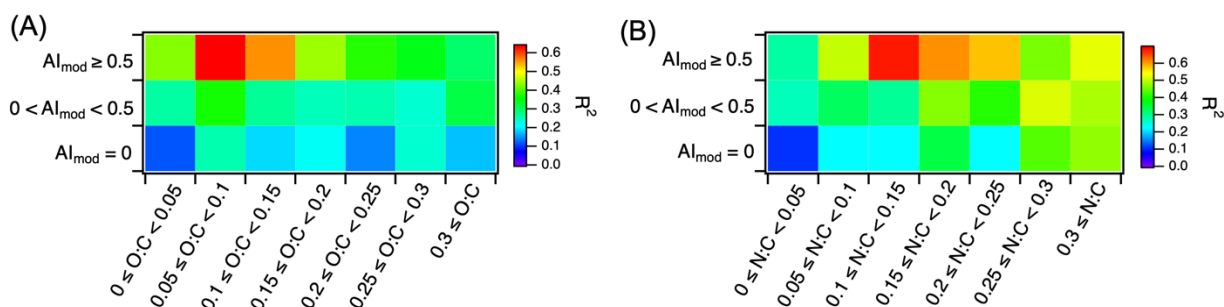
442

443

444



445



446 **Figure 4.** Heat maps of the coefficient of determination ( $R^2$ ) from linear regressions relating the mass-normalized DTT  
 447 consumption rate ( $OP_{DTTm}$ ) to the summed UHPLC–HRMS signal intensity of molecular-formula bins grouped by modified  
 448 aromaticity index ( $AI_{mod}$ ) and (A) oxygen-to-carbon (O:C) or (B) nitrogen-to-carbon (N:C) ratio, across fresh and ozone-aged  
 449 Bakhoor burning and cigarette smoke samples.

450

451

452

453

454

455

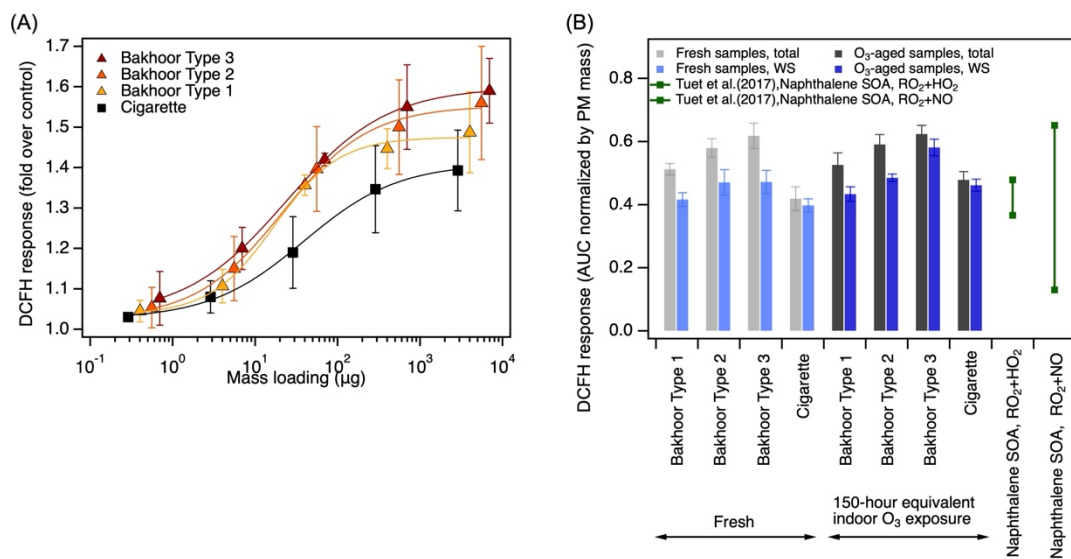
456

457

458



459



460

461 **Figure 5.** Intracellular oxidative-stress responses (DCFH assay) induced by particles from three Bakhoor types and sidestream  
 462 cigarette smoke. (A) Dose–response curves of DCFH fluorescence (reported as fold change relative to untreated controls) as  
 463 a function of particle mass loading; solid lines denote Hill-equation fits. (B) Integrated responses quantified as the area under  
 464 the fitted dose–response curve (AUC), normalized by particle mass, for fresh and  $\text{O}_3$ -aged samples and for total particle  
 465 suspensions and water-soluble (WS) extracts. Reference values for naphthalene SOA are from Tuet et al. (2017)

466

467

468

469

470

471

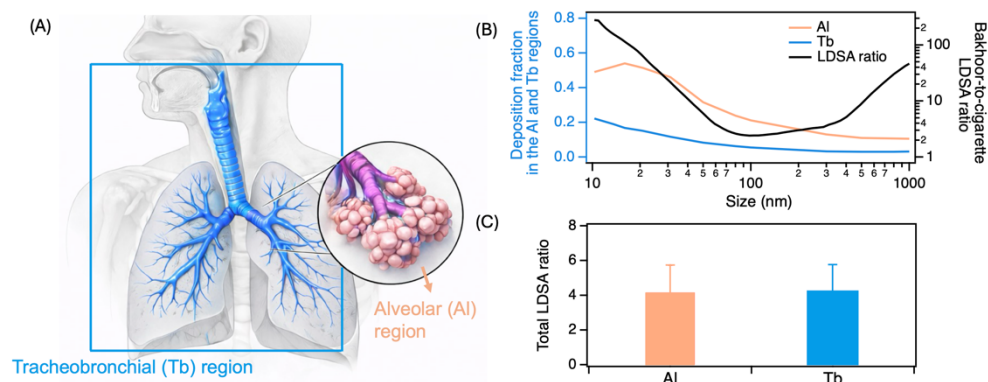
472

473

474



475



476

477 **Figure 6.** (A) Schematic of the human respiratory tract highlighting the tracheobronchial (Tb) and alveolar (Al) regions used  
478 for deposition calculations. (B) Size-resolved regional deposition fractions for the Tb and Al regions (left axis) and the  
479 corresponding size-resolved ratio of lung-deposited surface area (LDSA) for Bakhoor burning particles relative to sidestream  
480 cigarette smoke particles (right axis). (C) Bakhoor-to-cigarette LDSA ratio integrated over the measured particle size range  
481 for the Tb and Al regions; error bars denote  $\pm 1$  standard deviation ( $1\sigma$ ).

482

483

484

485

486



487

488 **Data availability.** All datasets used in this study, as well as the data products generated during the analysis, are available from  
489 the corresponding author upon request. These data are not publicly archived because they are maintained as multiple processed  
490 and analysis-specific files rather than as a repository-ready dataset.

491 **Author contributions.** CKC and LZ designed the experiment; LZ and ZL conducted the experiments; LZ, ZL and WX  
492 performed the data interpretation; LZ, ZL, WX, RJH and CKC wrote the paper. All authors contributed to the paper with useful  
493 scientific discussions or comments.

494 **Competing interests.** The contact author has declared that neither they nor their co-authors have any competing interests.

495 **Acknowledgements.** C.K.C. gratefully acknowledges support from the KAUST Baseline Research Fund (BAS/1/1432-01-  
496 01), the Center of Excellence for Smart Health (KCSH) Fund (award no. 5932) at King Abdullah University of Science and  
497 Technology, and the Hong Kong Research Grants Council (11304121 and 11314222).

498

499

500

## 501 **References**

502 Abbatt, J. P. D. and Wang, C.: The atmospheric chemistry of indoor environments, *Environmental Science: Processes &*  
503 *Impacts*, **22**, 25–48, 2020.

504 Alarifi, S. A., Mubarak, M. M., and Alokail, M. S.: Ultrastructural changes of pneumocytes of rat exposed to Arabian incense  
505 (Bakhour), *Saudi Medical Journal*, **25**, 1689–1693, 2004.

506 Brehmer, C., Lai, A., Clark, S., Shan, M., Ni, K., et al.: The oxidative potential of personal and household PM<sub>2.5</sub> in a rural  
507 setting in southwestern China, *Environmental Science & Technology*, **53**, 2788–2798, 2019.

508 Bu-Olayan, A. H. and Thomas, B. V.: Exposition of respiratory ailments from trace metals concentrations in incenses,  
509 *Scientific Reports*, **11**, 10210, <https://doi.org/10.1038/s41598-021-89493-w>, 2021.

510 Charrier, J. G. and Anastasio, C.: On dithiothreitol (DTT) as a measure of oxidative potential for ambient particles: Evidence  
511 for the importance of soluble transition metals, *Atmospheric Chemistry and Physics*, **12**, 11317–11350, 2012.

512 Chen, C. and Zhao, B.: Indoor emissions contributed the majority of ultrafine particles in Chinese urban residences,  
513 *Environmental Science & Technology*, **58**, 8444–8456, <https://doi.org/10.1021/acs.est.4c00556>, 2024.

514 Chen, K., Raeofy, N., Lum, M., Mayorga, R., Woods, M., et al.: Solvent effects on chemical composition and optical properties  
515 of extracted secondary brown carbon constituents, *Aerosol Science and Technology*, **56**, 917–930, 2022.

516 Cho, A. K., Sioutas, C., Miguel, A. H., Kumagai, Y., Schmitz, D. A., et al.: Redox activity of airborne particulate matter at  
517 different sites in the Los Angeles Basin, *Environmental Research*, **99**, 40–47, 2005.



- 518 Chuang, H.-C., BéruBé, K., Lung, S.-C. C., Bai, K.-J., and Jones, T.: Investigation into the oxidative potential generated by  
519 the formation of particulate matter from incense combustion, *Journal of Hazardous Materials*, **244–245**, 142–150,  
520 <https://doi.org/10.1016/j.jhazmat.2012.11.034>, 2013.
- 521 Cincinelli, A. and Martellini, T.: Indoor air quality and health, *International Journal of Environmental Research and Public  
522 Health*, **14**, 1286, 2017.
- 523 Dalibalta, S., Elsayed, Y., Alqtaishat, F., Gomes, I., and Fernandes, N.: A health risk assessment of Arabian incense (Bakhour)  
524 smoke in the United Arab Emirates, *Science of The Total Environment*, **511**, 684–691,  
525 <https://doi.org/10.1016/j.scitotenv.2014.12.024>, 2015.
- 526 Diapouli, E., Chaloulakou, A., and Koutrakis, P.: Estimating the concentration of indoor particles of outdoor origin: A review,  
527 *Journal of the Air & Waste Management Association*, **63**, 1113–1129, 2013.
- 528 Dou, J., Lin, P., Kuang, B.-Y., and Yu, J. Z.: Reactive oxygen species production mediated by humic-like substances in  
529 atmospheric aerosols: Enhancement effects by pyridine, imidazole, and their derivatives, *Environmental Science & Technology*,  
530 **49**, 6457–6465, <https://doi.org/10.1021/es5059378>, 2015.
- 531 Elsayed, Y., Dalibalta, S., Gomes, I., Fernandes, N., and Alqtaishat, F.: Chemical composition and potential health risks of  
532 raw Arabian incense (Bakhour), *Journal of Saudi Chemical Society*, **20**, 465–473, 2016.
- 533 Escalante, J., Chen, W.-H., Tabatabaei, M., Hoang, A. T., Kwon, E. E., et al.: Pyrolysis of lignocellulosic, algal, plastic, and  
534 other biomass wastes for biofuel production and circular bioeconomy: A review of thermogravimetric analysis (TGA)  
535 approach, *Renewable and Sustainable Energy Reviews*, **169**, 112914, 2022.
- 536 Fang, T., Zeng, L., Gao, D., Verma, V., Stefaniak, A. B., et al.: Ambient size distributions and lung deposition of aerosol  
537 dithiothreitol-measured oxidative potential: Contrast between soluble and insoluble particles, *Environmental Science &  
538 Technology*, **51**, 6802–6811, 2017.
- 539 Fang, T., Hwang, B. C., Kapur, S., Hopstock, K. S., Wei, J., et al.: Wildfire particulate matter as a source of environmentally  
540 persistent free radicals and reactive oxygen species, *Environmental Science: Atmospheres*, **3**, 581–594, 2023.
- 541 Fritz, K. S. and Petersen, D. R.: An overview of the chemistry and biology of reactive aldehydes, *Free Radical Biology and  
542 Medicine*, **59**, 85–91, 2013.
- 543 Gao, D., Fang, T., Verma, V., Zeng, L., and Weber, R. J.: A method for measuring total aerosol oxidative potential (OP) with  
544 the dithiothreitol (DTT) assay and comparisons between an urban and roadside site of water-soluble and total OP, *Atmospheric  
545 Measurement Techniques*, **10**, 2821–2835, 2017.
- 546 Gligorovski, S. and Abbatt, J. P. D.: An indoor chemical cocktail, *Science*, **359**, 632–633,  
547 <https://doi.org/10.1126/science.aar6837>, 2018.
- 548 Go, B. R., Lyu, Y., Ji, Y., Li, Y. J., Huang, D. D., et al.: Aqueous secondary organic aerosol formation from the direct  
549 photosensitized oxidation of vanillin in the absence and presence of ammonium nitrate, *Atmospheric Chemistry and Physics*,  
550 **22**, 273–293, 2022.
- 551 Hofmann, W.: Modelling inhaled particle deposition in the human lung—A review, *Journal of Aerosol Science*, **42**, 693–724,  
552 2011.
- 553 Hu, H., Ye, J., Liu, C., Yan, L., Yang, F., et al.: Emission and oxidative potential of PM<sub>2.5</sub> generated by nine indoor sources,  
554 *Building and Environment*, **230**, 110021, 2023.



- 555 Indraganti, M., Boussaa, D., and Asadi, S.: Necessity of the adaptive comfort standard for the Middle East in the times of  
556 rising energy use, *Qatar Foundation Annual Research Conference Proceedings*, **EEPP3015**, 2016.
- 557 Isenor, B. H., Varnaite, G., Jeong, C.-H., Subramanian, P. G., Duruisseau-Kuntz, R., et al.: Impacts of the 2023 Canadian  
558 wildfires on the oxidative potential of particulate matter, *ACS ES&T Air*, **2**, 2238–2250, 2025.
- 559 Jareebi, M. A., Alqassim, A. Y., Almrayisi, S. A., Alfaifi, W. A., Masri, T. A., et al.: Exploring the relationship between  
560 Bakhour use and respiratory health: A cross-sectional study in the Jazan Region, Saudi Arabia, *International Journal of*  
561 *General Medicine*, **17**, 2833–2845, 2024.
- 562 Jetter, J. J., Guo, Z., McBrien, J. A., and Flynn, M. R.: Characterization of emissions from burning incense, *Science of The*  
563 *Total Environment*, **295**, 51–67, [https://doi.org/10.1016/S0048-9697\(02\)00043-8](https://doi.org/10.1016/S0048-9697(02)00043-8), 2002.
- 564 Jiang, H., Ahmed, C. S., Canchola, A., Chen, J. Y., and Lin, Y.-H.: Use of dithiothreitol assay to evaluate the oxidative potential  
565 of atmospheric aerosols, *Atmosphere*, **10**, 571, 2019.
- 566 Jiang, J., Jung, N., and Boor, B. E.: Using building energy and smart thermostat data to evaluate indoor ultrafine particle source  
567 and loss processes in a net-zero energy house, *ACS ES&T Engineering*, **1**, 780–793, 2021.
- 568 Kim, M., Han, C. H., and Lee, M. Y.: NADPH oxidase and the cardiovascular toxicity associated with smoking, *Toxicological*  
569 *Research*, **30**, 149–157, <https://doi.org/10.5487/TR.2014.30.3.149>, 2014.
- 570 Koch, B. P. and Dittmar, T.: From mass to structure: An aromaticity index for high-resolution mass data of natural organic  
571 matter, *Rapid Communications in Mass Spectrometry*, **20**, 926–932, 2006.
- 572 Kuye, A. and Kumar, P.: A review of the physicochemical characteristics of ultrafine particle emissions from domestic solid  
573 fuel combustion during cooking and heating, *Science of The Total Environment*, **886**, 163747, 2023.
- 574 Lai, R. W. S., Qiu, T., Zhang, X., Wang, Y., Hao, T., et al.: Deciphering the key drivers of oxidative potential during  
575 ammonium nitrate-mediated aqueous-phase photoreaction of methoxyphenols, *Atmospheric Environment*, **340**, 120895,  
576 <https://doi.org/10.1016/j.atmosenv.2024.120895>, 2025.
- 577 Liang, Z., Zhou, L., Chang, Y., Qin, Y., and Chan, C. K.: Biomass-burning organic aerosols as a pool of atmospheric reactive  
578 triplets to drive multiphase sulfate formation, *Proceedings of the National Academy of Sciences*, **121**, e2416803121, 2024.
- 579 Liu, F., Whitley, J., Ng, N. L., and Lu, H.: Time-resolved single-cell assay for measuring intracellular reactive oxygen species  
580 upon exposure to ambient particulate matter, *Environmental Science & Technology*, **54**, 13121–13130,  
581 <https://doi.org/10.1021/acs.est.0c02889>, 2020a.
- 582 Liu, F., Saavedra, M. G., Champion, J. A., Griendling, K. K., and Ng, N. L.: Prominent contribution of hydrogen peroxide to  
583 intracellular reactive oxygen species generated upon exposure to naphthalene secondary organic aerosols, *Environmental*  
584 *Science & Technology Letters*, **7**, 171–177, <https://doi.org/10.1021/acs.estlett.9b00773>, 2020b.
- 585 Liu, F., Joo, T., Ditto, J. C., Saavedra, M. G., Takeuchi, M., et al.: Oxidized and unsaturated: Key organic aerosol traits  
586 associated with cellular reactive oxygen species production in the southeastern United States, *Environmental Science &*  
587 *Technology*, **57**, 14150–14161, <https://doi.org/10.1021/acs.est.3c03641>, 2023.
- 588 Liu, X., Testa, B., and Fahr, A.: Lipophilicity and its relationship with passive drug permeation, *Pharmaceutical Research*, **28**,  
589 962–977, 2011.
- 590 LoPachin, R. M. and Gavin, T.: Molecular mechanisms of aldehyde toxicity: A chemical perspective, *Chemical Research in*  
591 *Toxicology*, **27**, 1081–1091, <https://doi.org/10.1021/tx5001046>, 2014.



- 592 Lyu, Y., Guo, H., Cheng, T., and Li, X.: Particle size distributions of oxidative potential of lung-deposited particles: Assessing  
593 contributions from quinones and water-soluble metals, *Environmental Science & Technology*, **52**, 6592–6600, 2018.
- 594 Nazaroff, W. W. and Weschler, C. J.: Indoor ozone: Concentrations and influencing factors, *Indoor Air*, **32**, e12942, 2022.
- 595 Oberdörster, G., Oberdörster, E., and Oberdörster, J.: Nanotoxicology: An emerging discipline evolving from studies of  
596 ultrafine particles, *Environmental Health Perspectives*, **113**, 823–839, 2005.
- 597 Oh, H.-J., Chen, Y., and Kim, H.: Deposition of secondary organic aerosol in human lung model: Effect of photochemically  
598 aged aerosol on human respiratory system, *Ecotoxicology and Environmental Safety*, **265**, 115497, 2023.
- 599 Ott, W. R., Zhao, T., Cheng, K.-C., Wallace, L. A., and Hildemann, L. M.: Measuring indoor fine particle concentrations,  
600 emission rates, and decay rates from cannabis use in a residence, *Atmospheric Environment: X*, **10**, 100106,  
601 <https://doi.org/10.1016/j.aecoa.2021.100106>, 2021.
- 602 Pan, A., Clark, M. L., Ang, L.-W., Yu, M. C., Yuan, J.-M., et al.: Incense use and cardiovascular mortality among Chinese in  
603 Singapore: The Singapore Chinese Health Study, *Environmental Health Perspectives*, **122**, 1279–1284, 2014.
- 604 Park, J.-H., Troxel, A. B., Harvey, R. G., and Penning, T. M.: Polycyclic aromatic hydrocarbon (PAH) o-quinones produced  
605 by the aldo-keto reductases (AKRs) generate abasic sites, oxidized pyrimidines, and 8-oxo-dGuo via reactive oxygen species,  
606 *Chemical Research in Toxicology*, **19**, 719–728, <https://doi.org/10.1021/tx0600245>, 2006.
- 607 Patriarca, C., Bergquist, J., Sjoberg, P. J., Tranvik, L., and Hawkes, J. A.: Online HPLC-ESI-HRMS method for the analysis  
608 and comparison of different dissolved organic matter samples, *Environmental Science & Technology*, **52**, 2091–2099, 2018.
- 609 Pillariseti, A., Ye, W., and Chowdhury, S.: Indoor air pollution and health: Bridging perspectives from developing and  
610 developed countries, *Annual Review of Environment and Resources*, **47**, 197–229, [https://doi.org/10.1146/annurev-environ-](https://doi.org/10.1146/annurev-environ-012220-010602)  
611 [012220-010602](https://doi.org/10.1146/annurev-environ-012220-010602), 2022.
- 612 Sadoun, E. T., Fthenou, E., Kakosimos, K. E., Saraga, D., and Maggos, T.: Chemical characterization of indoor and outdoor  
613 PM<sub>2.5</sub>, PM<sub>10</sub> and VOCs in a public building in Doha City, Qatar, *Qatar Foundation Annual Research Conference*  
614 *Proceedings*, **EEPP1931**, 2016.
- 615 Salthammer, T.: Critical evaluation of approaches in setting indoor air quality guidelines and reference values, *Chemosphere*,  
616 **82**, 1507–1517, <https://doi.org/10.1016/j.chemosphere.2010.11.023>, 2011.
- 617 Seo, J., Kim, H., Park, E., Woo, J., and Lee, K.-H.: Source and condition specific toxicity of combustion-derived PM: Linking  
618 physicochemical properties with acellular and cellular assays, *Journal of Hazardous Materials*, **139344**, 2025.
- 619 Shen, G., Gaddam, C. K., Ebersviller, S. M., Vander Wal, R. L., Williams, C., et al.: A laboratory comparison of emission  
620 factors, number size distributions, and morphology of ultrafine particles from 11 different household cookstove-fuel systems,  
621 *Environmental Science & Technology*, **51**, 6522–6532, 2017.
- 622 Shultz, C. A., Quinn, A. M., Park, J.-H., Harvey, R. G., Bolton, J. L., et al.: Specificity of human aldo-keto reductases,  
623 NAD(P)H:quinone oxidoreductase, and carbonyl reductases to redox-cycle polycyclic aromatic hydrocarbon diones and 4-  
624 hydroxyequilenin-o-quinone, *Chemical Research in Toxicology*, **24**, 2153–2166, 2011.
- 625 Smith, J. S., Laskin, A., and Laskin, J.: Molecular characterization of biomass burning aerosols using high-resolution mass  
626 spectrometry, *Analytical Chemistry*, **81**, 1512–1521, 2009.
- 627 Song, J., Li, M., Zou, C., Cao, T., Fan, X., et al.: Molecular characterization of nitrogen-containing compounds in humic-like  
628 substances emitted from biomass burning and coal combustion, *Environmental Science & Technology*, **56**, 119–130, 2021.



- 629 Song, J., Li, M., Fan, X., Zou, C., Zhu, M., et al.: Molecular characterization of water- and methanol-soluble organic  
630 compounds emitted from residential coal combustion using ultrahigh-resolution electrospray ionization Fourier transform ion  
631 cyclotron resonance mass spectrometry, *Environmental Science & Technology*, **53**, 13607–13617, 2019.
- 632 Tian, Y., Arata, C., Boedicker, E., Lunderberg, D. M., Patel, S., et al.: Indoor emissions of total and fluorescent supermicron  
633 particles during HOMEChem, *Indoor Air*, **31**, 88–98, <https://doi.org/10.1111/ina.12731>, 2021.
- 634 Tuet, W. Y., Chen, Y., Fok, S., Gao, D., Weber, R. J., et al.: Chemical and cellular oxidant production induced by naphthalene  
635 secondary organic aerosol (SOA): Effect of redox-active metals and photochemical aging, *Scientific Reports*, **7**, 15157, 2017.
- 636 Tuet, W. Y., Fok, S., Verma, V., Rodriguez, M. S. T., Grosberg, A., et al.: Dose-dependent intracellular reactive oxygen and  
637 nitrogen species (ROS/RNS) production from particulate matter exposure: Comparison to oxidative potential and chemical  
638 composition, *Atmospheric Environment*, **144**, 335–344, 2016.
- 639 Tuet, W. Y., Liu, F., de Oliveira Alves, N., Fok, S., Artaxo, P., et al.: Chemical oxidative potential and cellular oxidative stress  
640 from open biomass burning aerosol, *Environmental Science & Technology Letters*, **6**, 126–132,  
641 <https://doi.org/10.1021/acs.estlett.9b00060>, 2019.
- 642 Wahab, A. A. and Mostafa, O. A.: Arabian incense exposure among Qatari asthmatic children: A possible risk factor, *Saudi  
643 Medical Journal*, **28**, 476–478, 2007.
- 644 Wang, C., Collins, D. B., Hems, R. F., Borduas, N., Antiñolo, M., et al.: Exploring conditions for ultrafine particle formation  
645 from oxidation of cigarette smoke in indoor environments, *Environmental Science & Technology*, **52**, 4623–4631, 2018a.
- 646 Wang, K., Huang, R.-J., Brüggemann, M., Zhang, Y., Yang, L., et al.: Urban organic aerosol composition in eastern China  
647 differs from north to south: Molecular insight from a liquid chromatography–mass spectrometry (Orbitrap) study, *Atmospheric  
648 Chemistry and Physics*, **21**, 9089–9104, 2021.
- 649 Wang, S., Ye, J., Soong, R., Wu, B., Yu, L., et al.: Relationship between chemical composition and oxidative potential of  
650 secondary organic aerosol from polycyclic aromatic hydrocarbons, *Atmospheric Chemistry and Physics*, **18**, 3987–4003, 2018b.
- 651 Wang, S., Gallimore, P. J., Liu-Kang, C., Yeung, K., Campbell, S. J., et al.: Dynamic wood smoke aerosol toxicity during  
652 oxidative atmospheric aging, *Environmental Science & Technology*, **57**, 1246–1256, 2023.
- 653 Wang, X. and Chan, A. W.: Particulate matter and volatile organic compound emissions generated from a domestic air fryer,  
654 *Environmental Science & Technology*, **57**, 17384–17392, 2023.
- 655 Wong, J. P., Tsagkaraki, M., Tsiodra, I., Mihalopoulos, N., Violaki, K., et al.: Effects of atmospheric processing on the  
656 oxidative potential of biomass burning organic aerosols, *Environmental Science & Technology*, **53**, 6747–6756, 2019.
- 657 Wu, C. L., Chao, C. Y. H., Sze-To, G. N., Wan, M. P., and Chan, T. C.: Ultrafine particle emissions from cigarette smouldering,  
658 incense burning, vacuum cleaner motor operation and cooking, *Indoor and Built Environment*, **21**, 782–796,  
659 <https://doi.org/10.1177/1420326X11421356>, 2012.
- 660 Xiong, Q., Yu, H., Wang, R., Wei, J., and Verma, V.: Rethinking dithiothreitol-based particulate matter oxidative potential:  
661 Measuring dithiothreitol consumption versus reactive oxygen species generation, *Environmental Science & Technology*, **51**,  
662 6507–6514, 2017.
- 663 Yeatts, K. B., El-Sadig, M., Leith, D., Kalsbeek, W., Al-Maskari, F., et al.: Indoor air pollutants and health in the United Arab  
664 Emirates, *Environmental Health Perspectives*, **120**, 687–694, 2012.



- 665 Yuan, W., Zhang, L., Zhao, W., Yang, B., Jiao, X., et al.: Multiphase reaction of ozone with HONO/NO<sub>2</sub><sup>-</sup> on surfaces: Effects  
666 on indoor HONO and ozone, *Environmental Science & Technology*, **59**, 7246–7255, 2025.
- 667 Zhang, L., Li, Y., Li, J., Xing, R., Liu, X., et al.: Pollutant emissions and oxidative potentials of particles from the indoor  
668 burning of biomass pellets, *Environmental Science & Technology*, **58**, 16016–16027, 2024.
- 669 Zhang, Y., McMurry, P. H., Yu, F., and Jacobson, M. Z.: A comparative study of nucleation parameterizations: 1. Examination  
670 and evaluation of the formulations, *Journal of Geophysical Research: Atmospheres*, **115**, 2010.
- 671 Zhao, L. and Liu, J.: Operating behavior and corresponding performance of mechanical ventilation systems in Chinese  
672 residential buildings, *Building and Environment*, **170**, 106600, <https://doi.org/10.1016/j.buildenv.2019.106600>, 2020.
- 673 Zhao, W., Jiao, X., Xie, Y., Liu, T., Zhou, L., et al.: Impact of mosquito-repellent incense emissions and aging processes in  
674 the indoor environment, *ACS ES&T Air*, **2**, 2659–2668, 2025.